nature communications

Article

https://doi.org/10.1038/s41467-025-59830-y

Water-shielding electric double layer and stable interphase engineering for durable aqueous zinc-ion batteries

Received: 28 August 2024

Accepted: 5 May 2025

Published online: 14 May 2025

Check for updates

Zhongyou Peng[1], Shulong Li[1], Ling Tang[1], Jinyang Zheng[1], Licheng Tan[1] ✉ & Yiwang Chen[1,2] ✉

Aqueous zinc-ion batteries persistently encounter interface issues stemming from the water-rich electrical double layer and unstable solid-electrolyte interphase, drastically compromising reversibility and cyclability. Here we show that trace amounts of nonionic amphiphilic polysorbate additives promote the formation of water-shielding electric double layer and stabilize solid-electrolyte interphase for practical zinc-ion batteries. We demonstrate that polysorbate molecules can produce preferential chemisorption and directional arrangement on the Zn anode, spontaneously forming water-shielding layer to suppress the water-related side reactions. Simultaneously, polysorbate molecules can assist the construction of organic-inorganic hybrid interphase, which effectively regulates the uniform distribution of electric field and guides preferential orientation Zn deposition to achieve ordered plating/stripping with high Zn utilization. Consequently, the polysorbate-containing electrolyte enables a long cycle life of 8060 h at 1 mA cm^{-2}, 1 mAh cm^{-2} for Zn||Zn cell, and highly reversible Zn plating/stripping in Zn||Cu cell over 3900 cycles. The full cells paired with V_2O_5/rGO and MnO_2 deliver the improved capacity and sustained stability.

Rechargeable aqueous zinc-ion batteries (ZIBs) have been considered as transformative candidates for broad-scale energy storage applications, primarily driven by the exceptional merits of metallic zinc (Zn) anodes. These advantages encompass high theoretical capacities (820 mAh g^{-1} and 5855 mAh cm^{-3}), competitive electrochemical potential (−0.762 V *vs* the standard hydrogen electrode), satisfactory natural abundance, and low cost[1–4]. Moreover, the inherent chemical stability and intrinsic safety profile of Zn metal further position it as an ideal anode material for developing economical and energy-dense aqueous battery systems. Nevertheless, the commercialization of ZIBs is impeded by interfacial degradation cascades: rampant growth of Zn dendrites, inevitable corrosion reactions, parasitic hydrogen evolution reaction (HER), and inefficient Zn utilization, collectively depressing Coulombic efficiency (CE) and cycle life below industrial thresholds[5,6]. Generally speaking, chemical corrosion and parasitic reactions of Zn anode by water-rich electrical double layer (EDL) and water-decomposition dominated solid-electrolyte interface (SEI) account for the unstable and irreversible ZIBs, especially under harsh conditions[7]. This interfacial instability mandates excessive anode thickness to offset irreversible Zn consumption, directly compromising system-level energy density and cost-effectiveness[8]. Under such circumstances, it is essential and indispensable to develop ZIBs with highly reversible and stable Zn chemistry for practical applications.

Extensive research efforts have devoted to optimize the stability and reversibility of Zn anodes from the point of view of structure modification (Zn powder[9,10], Zn alloy[11], Zn foil[12,13], 3D architectures[14]), separator modification (cellulose nanofiber films[15,16], glass fiber films[17], polytetrafluoroethylene membrane[18], polyethylene membrane[19]),

[1]College of Chemistry and Chemical Engineering/Institute of Polymers and Energy Chemistry (IPEC)/Film Energy Chemistry for Jiangxi Provincial Key Laboratory (FEC), Nanchang University, Nanchang, China. [2]College of Chemistry and Chemical Engineering, Gannan Normal University, Ganzhou, China. ✉e-mail: tanlicheng@ncu.edu.cn; ywchen@ncu.edu.cn

protective coatings modification (ex situ construction[20], in situ construction[21]), electrolytes optimization (functional additives[22], high-concentration electrolytes[23], eutectic electrolytes[24], hydrogel electrolytes[25]), etc. Among these, electrolyte additives have proved to be effective in modulating Zn^{2+} solvation structures and suppressing water reactivity, thereby enabling dendrite-free deposition. Moreover, constructing a reliable and sustainable SEI on the Zn anode surface has been identified as an effective strategy to prevent successive parasitic reactions and regulate zinc deposition[26,27]. Notably, conventional aqueous electrolytes in ZIBs inherently lack passivation agents, necessitating high-concentration electrolytes to force anion/solvent decomposition for SEI formation[28]. Despite the boosted electrochemical performance, these systems suffer from the high-cost, retarded interfacial reaction kinetics, and limited cyclability. Alternatively, a low dose of unstable additives was used to build in situ SEIs via spontaneous chemical reaction[29,30], but the resulting SEI in these works is often fragile and thin, unable to support long-term Zn stripping/plating. Furthermore, the stringent energy density requirements of the cell level need available zinc utilization (commonly referred to as depth of discharge (DOD_{Zn})) to be further increased to >50%, and the irreversibility issue at high DODs is rarely addressed. Noteworthily, recent insights reveal that EDL characteristics could manipulate the interfacial water activity and Zn^{2+} diffusion, and desolvation on the Zn anode surface, as well as actuate the formation of the in situ SEIs. Therefore, shedding more light on the correlation between EDL structure and SEI properties is important and could potentially enable the formation of a stable SEI via water-shielding EDL.

Here, we propose to trace large-sized nonionic amphiphilic polysorbate (denoted as PS) as a functional additive to engineer water-shielding EDL and organic-inorganic hybrid SEI for practical ZIBs. PS molecules leverage zincophilic oxygen-containing groups and hydrophobic long carbon chain to selectively disrupt interfacial hydrogen-bond networks, suppressing water activity while preserving native Zn^{2+} solvation structures (Supplementary Fig. 1). Both theoretical calculations and experimental tests have demonstrated that PS molecules could produce preferential chemisorption on the Zn surface and form the directional arrangement at the Zn/electrolyte interface, which is able to spontaneously build water-shielding EDL to suppress corrosion reactions and parasitic HER. Additionally, PS can assist the Zn anode surface to form a stable organic-inorganic hybrid SEI, facilitating the uniform distribution of the electric field and the homogeneous nucleation of Zn, which can further guide the preferential orientation of Zn (002) deposition and suppress side reactions. Consequently, the assembled Zn||Zn cell achieves a high rate from 1 to 40 mA cm^{-2} and a cycling stability for 8060 h under 1 mA cm^{-2}, 1 mAh cm^{-2} (450 h at 40 mA cm^{-2}, 40 mAh cm^{-2}). Moreover, the integrated Zn||Cu cell shows a high level of Coulombic efficiency (CE) of 99.2% with cycling durability over 3900 cycles. Full cells paired with V_2O_5/rGO and MnO_2 cathodes demonstrate improved zinc-ion storage capacity and sustained stability, demonstrating broad applicability.

Results

Characterization and simulation of electrolytes

We employ the nonionic amphiphilic polysorbate (PS, structure in Supplementary Fig. 2) as a functional additive to stabilize the Zn anode and investigate its mechanism of action. In baseline 1 M $Zn(OTf)_2$ electrolyte, a water-rich EDL exacerbates in the severe interface issues of HER, chemical corrosion, and dendritic growth (Fig. 1a). Upon the introduction of PS additive, PS molecules could produce preferential chemisorption and directional arrangement on the Zn anode, spontaneously forming water-shielding EDL and assisting in situ construction of stable organic and inorganic hybrid SEI. The synergistic effects of EDL and SEI significantly suppress water-related side reactions and effectively homogenize the distribution of solvated Zn^{2+}, tailoring the Zn^{2+} diffusion flux, achieving ordered planar plating/stripping. Electrostatic potential (ESP) analysis confirms oxygen atoms in PS serve as nucleophilic sites for Zn^{2+} coordination (Supplementary Fig. 3), while electrolyte compatibility tests reveal stable formulations across all PS concentrations (Supplementary Fig. 4). Critically, linear sweep voltammetry (LSV) shows that PS additive affords reduced hydrogen evolution reaction (HER) potential and increased oxygen evolution reaction (OER) potential (Supplementary Fig. 5), indicating that the PS additive possesses the positive effect on suppressing water decomposition.

Nuclear magnetic resonance (NMR), Raman, and Fourier transform infrared spectroscopy (FTIR) were measured to characterize the electrolyte bulk phase. Unlike it commonly occurs in the presence of an electrolyte additive, there is no significant difference in the ^{67}Zn (Fig. 1b) and ^{17}O (Fig. 1c) resonances of 1 M $Zn(OTf)_2$ electrolytes with various concentrations of PS, revealing that PS additive is not likely to affect the solvation structure of hydrated Zn^{2+}. Meanwhile, there is no obvious variation of FTIR peaks $\upsilon(S=O)$, $\upsilon(C-F)$ (Fig. 1d and Supplementary Fig. 6a) and Raman peaks $\upsilon(SO_3)$, $\upsilon(CF_3)$, $\upsilon(Zn-O)$ (Fig. 1e and Supplementary Fig. 6b) of 1 M $Zn(OTf)_2$ electrolytes with various concentrations of PS, which proves that Zn^{2+} still maintains a primary solvated structure and PS molecule is difficult to manipulate Zn^{2+} solvation sheath[31]. Noteworthily, the blue shift of $\nu(O-H)$ peaks indicates the increased interaction between PS and H_2O molecules, thus reconstructing the hydrogen-bond interaction between H_2O and PS, and further suppressing the activity of water molecules. Moreover, Zn||Cu cell optimization identifies 1 *wt*% PS as optimal, achieving 99.2% CE over 3900 cycles (Supplementary Fig. 7). Molecular dynamics (MD) simulations were performed to further explore the solvation structure, and MD trajectories are provided in Supplementary Data 1–4. In the 1 M $Zn(OTf)_2$ electrolyte, the strong distribution peak of Zn-H_2O appears at 1.92 Å, while the Zn-OTf^- distribution peak with weak intensity is located at 1.88 Å (Supplementary Fig. 8), which suggests that the Zn^{2+} cations prefer to be solvated by water. As indicated by the coordination numbers (CNs), Zn^{2+} inner solvation shell contains on average 5.5 H_2O molecules and 0.5 OTf^- anions. In the electrolyte with 1 *wt*% PS, Zn^{2+}-H_2O and Zn-OTf^- peaks share the same location, and a very weak peak of Zn^{2+}-PS distribution with a very low coordination number (0.008) occurs at 1.96 Å (Fig. 1f, g), indicating weak interaction between PS and Zn^{2+}. The almost unchanged H_2O and OTf^- number in the Zn^{2+} inner solvation shell suggests the PS does not alter Zn^{2+} inner solvation structure[32]. Besides, the X-ray adsorption fine structure (XAFS) (Fig. 1h) further verifies unchanged Zn^{2+} electronic states and local coordination[33,34]. The similar Fourier transformation of extended X-ray absorption fine structure (EXAFS) spectra (Fig. 1i and Supplementary Fig. 9) and wavelet transform of EXAFS spectra (Fig. 1j) show weak interaction between PS and Zn^{2+} rather than strong coordination. This collective evidence establishes that PS has little effect on Zn^{2+} solvation due to steric bulk and trace concentration, instead operating exclusively through interfacial H_2O sequestration.

The Zeta potential value increases from −7.89 to −2.03 mV after the addition of PS, indicating the stronger electrostatic adsorption on Zn surface (Fig. 1k). Compared with the contact angle of 82.6° in 1 M $Zn(OTf)_2$ electrolyte (I), the contact angle between Zn foil and PS-containing electrolyte (II) is reduced to 68.6° (Fig. 1l), which is conducive to improve the uniform distribution of Zn^{2+} flux. Intriguingly, the contact angle between 1 M $Zn(OTf)_2$ electrolyte and pre-soaked Zn foil (III) is much smaller than that on the bare Zn, which may be attributed to the by-product generated on the Zn metal. In contrast, the contact angle of Zn metal in the electrolyte with 1 *wt*% PS (IV) increased from 68.6° to 80.1°, revealing the partial hydrophobicity of the pre-soaked Zn foil surface. The hydrophobic tendency may be ascribed to the directional adsorption of the PS molecules on Zn metal, where zincophilic oxygen-containing functional groups are

https://doi.org/10.1038/s41467-025-59830-y

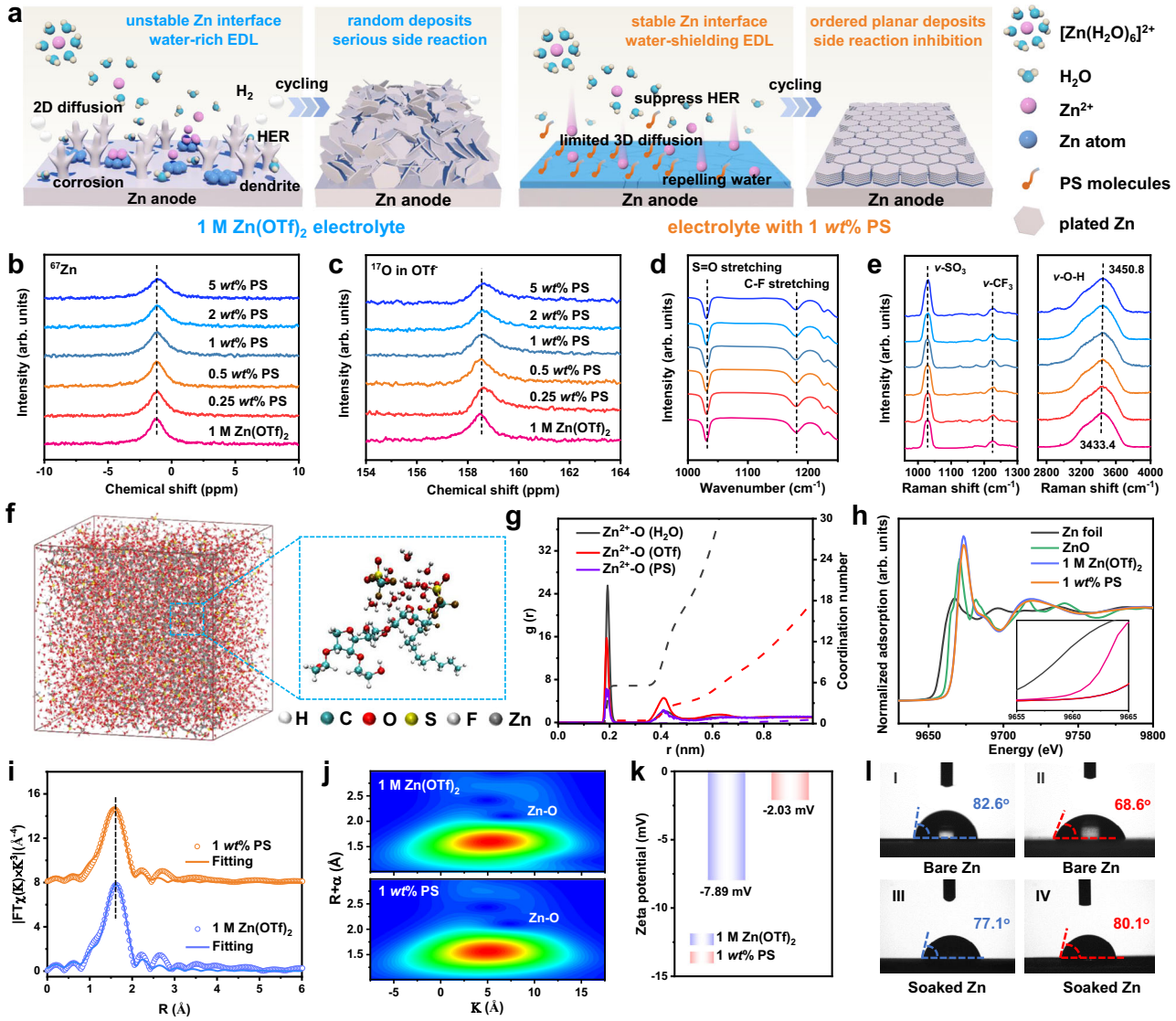

Fig. 1 | Characterization and simulation of electrolytes. a Schematic illustration of the effects of the PS molecule on electrolyte and interfacial chemistry for 1 M $Zn(OTf)_2$ electrolyte and electrolyte with 1 *wt*% PS. **b** ^{67}Zn NMR, **c** ^{17}O NMR in OTf^-, **d** FTIR spectra, and **e** Raman spectra of the 1 M $Zn(OTf)_2$ electrolytes with different concentrations of PS. **f** 3D snapshots of electrolyte with 1 *wt*% PS obtained from MD simulations, and the dashed profile is a partially enlarged snapshot for the solvation structure of Zn^{2+}. **g** The radial distribution functions and coordination number of Zn^{2+}-O collected from MD simulations. **h** Zn K-edge XANES spectra, and the intensity is normalized to the edge jump for quantitative comparison. **i** Fourier transform EXAFS curves and **j** Wavelet transforms of Zn K-edge XANES of 1 M $Zn(OTf)_2$ electrolyte and electrolyte with 1 *wt*% PS. **k** The Zeta potential of 1 M $Zn(OTf)_2$ electrolyte and electrolyte with 1 *wt*% PS. **l** Contact angles of 1 M $Zn(OTf)_2$ on bare Zn foil (I) and the Zn foil pre-soaked in 1 M $Zn(OTf)_2$ for 7 days (III), and contact angles of electrolyte with 1 *wt*% PS on bare Zn foil (II), and the Zn foil pre-soaked in electrolyte with 1 *wt*% PS for 7 days (IV).

preferentially adsorbed on the Zn anode, and the hydrophobic carbon chain points toward the electrolyte. The obvious C–O–C stretch vibration confirms the preferential adsorption behavior of PS molecules on the Zn anode surface (Supplementary Fig. 10a). X-ray diffraction (XRD) patterns (Supplementary Fig. 10b) and scanning electron microscopy (SEM) images (Supplementary Fig. 11) further indicate that obvious triflate hydroxide hydrate by-products appear on the Zn foil soaked in 1 M $Zn(OTf)_2$ electrolyte, while Zn foil soaked in the electrolyte with 1 *wt*% PS is clean without any protuberances. Furthermore, the lower corrosion current density and enhanced corrosion potential of the electrolyte with 1 *wt*% PS further affirm the alleviation of Zn corrosion reactions (Supplementary Fig. 12)[35]. These results collectively infer that the Zn metal surface-anchored PS molecules spontaneously form water-shielding EDL, simultaneously blocking H_2O access, thus suppressing water-induced side reactions and enhancing corrosion resistance.

Highly reversible Zn plating/stripping behavior

SEM and confocal laser scanning microscopy (CLSM) were used to study the structure evolution of Cu and Zn electrodes in the electrolytes with and without PS after the 50th plating. From Cu electrodes, 1 M $Zn(OTf)_2$ electrolyte induces dendritic Zn protrusions (Fig. 2a and Supplementary Fig. 13-15), while the electrolyte with 1 *wt*% PS yields compact, planar deposits. This morphological control correlates with larger nucleation overpotential (NOP) of the electrolyte with 1 *wt*% PS (97 mV), increased by 54 mV compared to the 1 M $Zn(OTf)_2$ electrolyte (Supplementary Fig. 16)[36,37]. Analogously, the Zn anode displays stepped morphology without aggregated by-products than those of the Zn anode in the 1 M $Zn(OTf)_2$ electrolyte (Fig. 2b and Supplementary Figs. 17–19), indicating that the PS additive enables uniform nucleation and regulates homogeneous Zn^{2+} deposition behavior. The surface geometry and potential of cycled Zn anodes in the electrolytes with and without PS were characterized by atomic force microscopy (AFM)

https://doi.org/10.1038/s41467-025-59830-y

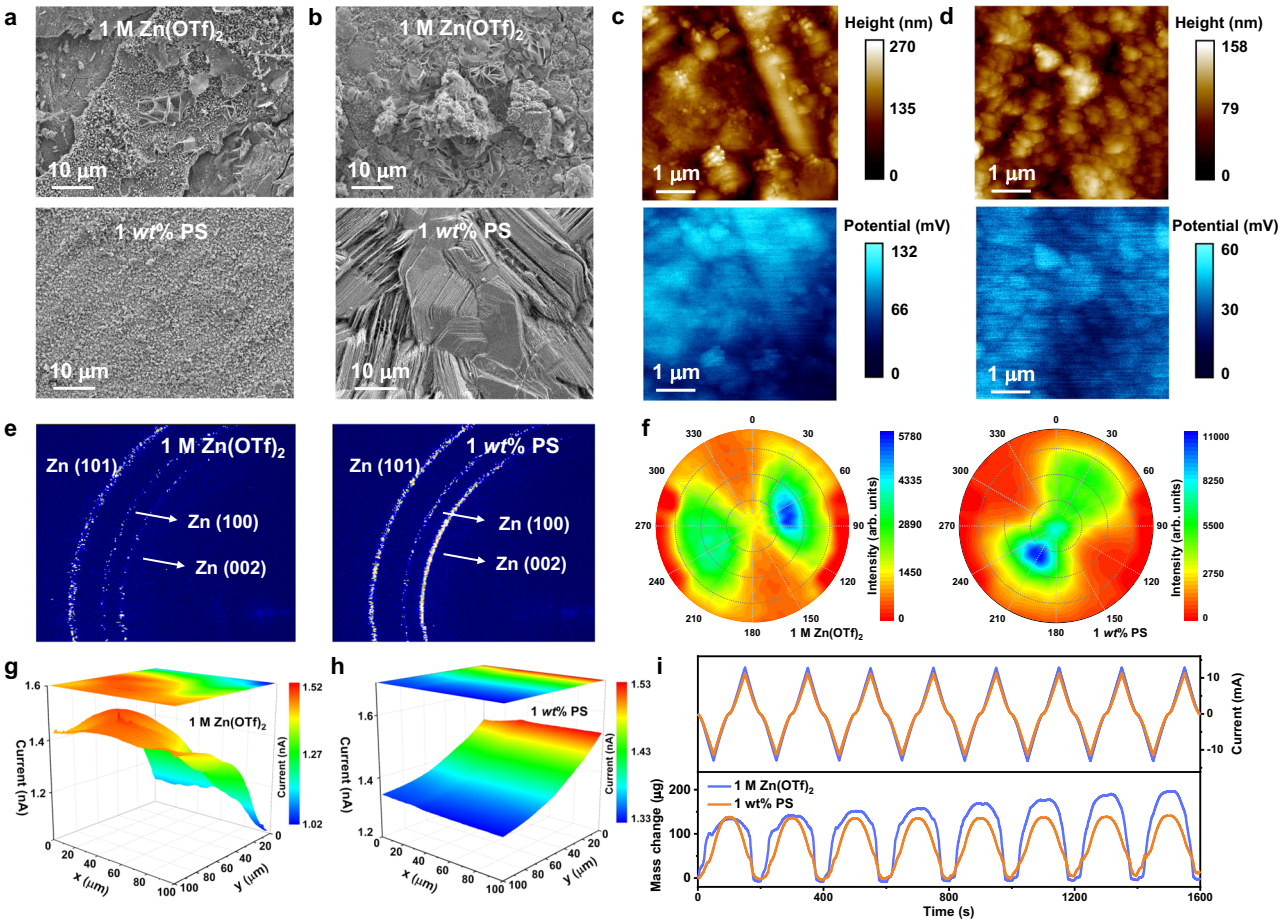

Fig. 2 | Impact of PS on Zn plating/stripping behavior. SEM images of **a** Cu electrodes and **b** Zn anodes in 1 M $Zn(OTf)_2$ electrolyte and electrolyte with 1 *wt*% PS after 50 cycles at 2 mA cm^{-2} and 2 mAh cm^{-2}. AFM and KPFM images of Zn anodes in (**c**) 1 M $Zn(OTf)_2$ electrolyte and (**d**) electrolyte with 1 *wt*% PS after 50 cycles at 2 mA cm^{-2} and 2 mAh cm^{-2}. **e** The 2D GIWAXS results and (**f**) (002) pole figures of Zn anodes in 1 M $Zn(OTf)_2$ electrolyte and electrolyte with 1 *wt*% PS after 50 cycles at 2 mA cm^{-2} and 2 mAh cm^{-2}. The change of feedback current by SECM area scan with the feedback mode on cycled Zn anode surface in (**g**) 1 M $Zn(OTf)_2$ electrolyte and (**h**) electrolyte with 1 *wt*% PS. **i** Chronocoulometry and mass changes based on EQCM in different electrolytes at a scan rate of 10 mV s^{-1}.

and Kelvin probe force microscopy (KPFM). The cycled Zn anode using 1 M $Zn(OTf)_2$ electrolyte exhibits a rough morphology with average height of 270.2 nm and high surface potential of 131.5 mV (Fig. 2c). In contrast, the Zn anode in the electrolyte with 1 *wt*% PS showcases a relatively flat surface morphology and even the distribution of electric field (Fig. 2d). Therefore, the PS can not only relieve electrochemical corrosion, but also organize Zn^{2+} deposition to obtain dendrite-free Zn anode.

Crystallographic evolution of cycled electrodes was probed via X-ray diffraction (XRD) and wide-angle XRD (WAXRD) pole figure analysis. The Cu electrode in 1 M $Zn(OTf)_2$ electrolyte appears to have evident peaks of side products indexed to $Zn_x(OTf)_{2x-y}$ H_2O (Supplementary Fig. 20a, b), which are not by-products in PS-containing electrolyte. Obviously, the diffraction peaks of the $CuZn_5$ phase are detected for the Cu electrode in the electrolyte with 1 *wt*% PS. As previously reported, this $CuZn_5$ phase is produced from the dissolution of Zn atoms into the Cu surface, which could regulate the Zn initial nuclei formation, compact growth of Zn, and suppress the dendrite growth[38–40]. From the Zn anode (Supplementary Fig. 20c), XRD patterns clearly confirm the presence of by-product in 1 M $Zn(OTf)_2$ electrolyte, while the electrolyte with 1 *wt*% PS retains phase purity. Moreover, the increase of peak intensity of the (002) plane for Zn anode in PS-containing electrolyte demonstrates that PS molecules can guide preferential orientation of Zn (002) deposition to achieve ordered planar plating/stripping. Moreover, both the Cu electrode and Zn anode in the electrolyte with 1 *wt*% PS exhibit flat and smooth surfaces after 50 cycles at 10 mA cm^{-2} and 10 mAh cm^{-2} (Supplementary Figs. 21 and 22). As shown in WAXRD pattern, three disordered Debye rings of cycled Zn anode clearly emerge in 1 M $Zn(OTf)_2$ electrolyte, representing (101), (100) and (002) planes (Fig. 2e). On the contrary, the deposited Zn in in the electrolyte with 1 *wt*% PS exhibits the highest diffraction intensity of (002) plane, indicating the preferred (002) plane growth[41,42]. Moreover, the higher pole intensity of the (002) texture with concentrated distribution for Zn cycled in the electrolyte with 1 *wt*% PS validates the prominent (002) plane growth (Fig. 2f and Supplementary Fig. 23). Previously reported results have demonstrated that the Zn anode with more exposed (002) planes can guide the Zn^{2+} deposition, and restrain chemical corrosion and HER activity[43].

Scanning electrochemical microscopy (SECM) quantified interfacial ion flux homogeneity using a four-electrode configuration (Supplementary Fig. 24a). In 1 M $Zn(OTf)_2$ electrolyte, the cycled Zn anode represents uneven electric field distribution and an obvious response current peak owing to tip-induced charge accumulation (Fig. 2g)[44,45]. However, the SECM image of the cycled Zn anode in the electrolyte with 1 *wt*% PS exhibits homogeneous electric field distribution and a minimal response current difference of 0.20 nA (Fig. 2h and Supplementary Fig. 24b), revealing highly uniform distribution of Zn^{2+} after the introduction of the PS, which effectively restrain the growth of Zn dendrites. Furthermore, in situ electrochemical quartz crystal microbalance (EQCM) combined with cyclic voltammetry (CV)

https://doi.org/10.1038/s41467-025-59830-y

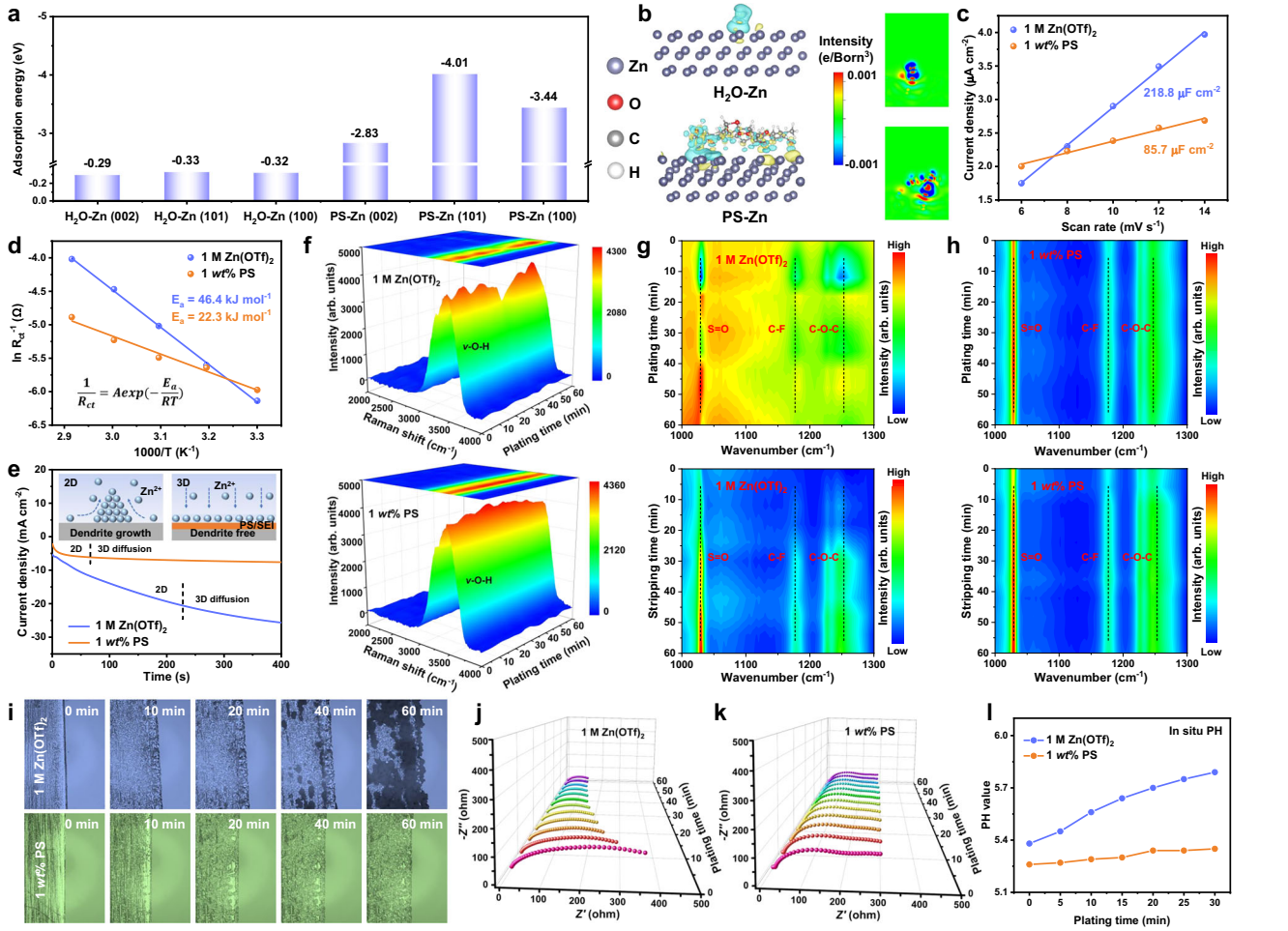

Fig. 3 | Stability and mechanism understanding of zinc anodes in $Zn(OTf)_2$ electrolyte with or without PS. a Absorption energy comparison of H_2O and PS molecules on different Zn crystal planes. **b** The charge density difference of H_2O and PS molecules on Zn (101) surface (yellow and blue semi-transparent clusters represent the electron accumulation and depletion, respectively). **c** Double layer capacitance at Zn electrode surface, **d** Arrhenius curves and comparison of activation energies, and (**e**) Chronoamperometry test of Zn electrode in 1 M $Zn(OTf)_2$ electrolyte and electrolyte with 1 *wt*% PS. Insets: schematics of the Zn^{2+} diffusion and deposition on the Zn anode. **f** Three-dimensional in situ Raman spectra of *υ*–O–H during Zn plating process, **g**, **h** In situ FTIR spectra of Zn plating/stripping process, **i** In situ optical microscopy images of Zn plating process, and in situ EIS of Zn||Zn symmetric cells during Zn plating process in (**j**) 1 M $Zn(OTf)_2$ electrolyte and (**k**) electrolyte with 1 *wt*% PS under 5 mA cm^{-2}. **l** Real-time pH variation near the surface of the Zn anode at 5 mA cm^{-2}.

was used to further verify the dynamic nature of the PS molecules, which accurately monitor the mass change of the working electrode during the Zn plating/stripping processes. Distinctly, the Zn anode in the electrolyte with 1 *wt*% PS shows the less mass gain in plating processes than 1 M $Zn(OTf)_2$ electrolyte, suggesting the improved reversibility (Fig. 2i). In addition, due to the accumulation of by-products on the Zn anode, the residual mass would increase with cycles in 1 M $Zn(OTf)_2$ electrolyte. The ratio of the mass change in the stripping process to the plating process in different electrolytes, denoted as the mass efficiency, can be used to relate the side reactions. Obviously, the mass efficiency of the electrolyte with 1 *wt*% PS always remains above 99.8%, which is higher than that of the 1 M $Zn(OTf)_2$ electrolyte. These results confirm that PS molecules can effectively suppress side reactions and improve reaction reversibility.

Mechanism understanding of the regulation of Zn electrodeposition

Density functional theory (DFT) calculations were applied to explore the adsorption mechanism and adsorption energies of PS/H_2O molecules on different Zn and Cu crystal planes. Coordinates for the optimized structure of PS are provided in Supplementary Data 5. Obviously, the adsorption energies of the PS molecule on Zn or Cu crystal planes are all lower than those of H_2O (Fig. 3a and Supplementary Fig. 25, 26), confirming a stronger Zn affinity and the preferential adsorption of PS molecule on Zn anode is conducive to reducing H_2O adsorption and suppress the HER simultaneously[46]. Compared with (002) Zn plane, PS molecule shows a higher adsorption energy (−2.83 eV) than (101) plane (−4.01 eV) and (100) plane (−3.44 eV) and will preferentially adsorb on (101) plane, then on (100) plane, while the (002) plane will be exposed. Zn metal with more exposed (002) planes could not only restrain the formation of dendrites kinetically, but also thermodynamically endow the most stable state, suppressing the side reactions due to the lowest surface energy. Similarly, the differential charge density distribution reveals the strong chemical adsorption of PS towards Zn anode, which may indicate that electrons are more inclined to transfer from PS to Zn during the constructed strong chemisorption process (Fig. 3b). PS restructures regulate the EDL structure and isolate water adsorption, reducing the electrical double layer capacitance from 218.8 to 85.7 μF cm^{-2} (Fig. 3c and Supplementary Fig. 27), consistent with in situ EQCM showing persistent PS adsorption (Supplementary Fig. 28)[47,48]. Furthermore, the electrolyte with 1 *wt*% PS exhibits a lower Zn^{2+} desolvation activation energy of 22.3 kJ mol^{-1} (Fig. 3d and Supplementary Fig. 29) and a higher Zn^{2+} transference number of 0.55 (Supplementary Fig. 30) compared

to the 1 M $Zn(OTf)_2$ electrolyte, suggesting that the PS anchoring layer apparently accelerates the desolvation process and further reduces water-related side reactions[49]. The desolvation energy of Zn^{2+} in the electrolyte with 1 *wt*% PS further demonstrates that the PS additive is beneficial to the desolvation and rapid ion transport of Zn^{2+} (Supplementary Fig. 31). Moreover, the Zn growth mechanism in different electrolytes was studied by chronoamperometry (CA) (Fig. 3e). The current density in 1 M $Zn(OTf)_2$ electrolyte continuously increases within 400 s, indicating the rampant and uncontrolled 2D diffusion process. As for the electrolyte with 1 *wt*% PS, a relatively constrained 2D diffusion and a longstanding 3D current diffusion in the subsequent process with a lower steady-state current response. This indicates that the adsorption of amphiphilic PS molecules on the Zn anode hinders the growth of the nucleus, facilitates uniform Zn deposition, and avoids the tip effect.

The in situ Raman spectroscopy was further employed to investigate the water-shielding EDL layer and the evolution of Zn deposition at the electrode/electrolyte interface. The peak width of O–H stretching vibration of H_2O molecules in 1 M $Zn(OTf)_2$ electrolyte shows an irregular evolution during the plating process, suggesting the nonuniformity of Zn^{2+} on the electrode/electrolyte interface (Fig. 3f and Supplementary Fig. 32), leading to hydrogen evolution and the formation of by-products[50]. The nearly constant peak intensity and width in the electrolyte with 1 *wt*% PS indicate the uniformity of the Zn^{2+} distribution and stability of the desolvated interfacial H_2O molecules. The considerable Raman signal at 1030 cm^{-1} deriving from OTf^- could be utilized to analyze the concentration changes of Zn^{2+}[51,52]. A obvious decay of the spectrum intensity in 1 M $Zn(OTf)_2$ electrolyte is determined during Zn plating, while the almost constant intensity of the Raman signal in the electrolyte with 1 *wt*% PS, which indicates that the introduction of PS can improve the consistency and uniformity of Zn^{2+} distribution (Supplementary Fig. 33a). Additionally, in 1 M $Zn(OTf)_2$ electrolyte, the concentration of H_2O and OTf^- at the zinc interface increases with electrode process due to the gradual desolvation of zinc ions. Furthermore, the regular and periodic intensity of the υ(Zn–O) peak in the electrolyte with 1 *wt*% PS further verifies the dynamic and stable adsorption/desorption behavior on the Zn anode surface (Supplementary Fig. 33b). Simultaneously, in situ FTIR spectra during plating and stripping processes were further studied for the analysis of the coordination environment and interfacial chemistry (Fig. 3g, h). During the plating and stripping process, the stretching vibration peaks of υ(S = O), υ(C–F), and υ(C–O–C) in the central region of 1 M $Zn(OTf)_2$ electrolyte experience unordered fluctuation, suggesting significant side reactions of active H_2O molecules and OTf^- anions at the Zn electrode/electrolyte interface[53]. Obviously, the uniform variation of the stretching vibration peaks definitively reveals the suppression of detrimental (electro-) chemical side reactions in the electrolyte with 1 *wt*% PS. Moreover, the observed change in the uniformity of the stretching vibration peaks of C–O–C confirm that the PS is able to move dynamically between the interfacial chemistry and coordination environment during plating/stripping (Supplementary Fig. 34). This spectroscopic validation further confirms that PS molecule derived water-shielding EDL layer is beneficial to improve the stability of interface chemistry and coordination environment.

The effect of PS on the Zn nucleation and deposition behavior is minutely recorded using in situ optical microscopy (Fig. 3i). 1 M $Zn(OTf)_2$ electrolyte fosters dendritic protrusions with vigorous HER, while the electrolyte with 1 *wt*% PS achieves planar deposition and near-complete HER suppression. In situ EIS of symmetric cells was further employed to investigate the interfacial electrochemical stability and the evolution of the Zn^{2+} transport kinetics (Fig. 3j, k). The precarious Zn/electrolyte interface in the 1 M $Zn(OTf)_2$ electrolyte exhibits a progressive decrease in interfacial impedance, originating from the fast electrochemical reduction kinetics of Zn^{2+}, causing nonuniform zinc deposition. In sharp contrast, the zinc anode in the electrolyte with 1 *wt*% PS undergoing continuous cycling sustains a stable interfacial impedance, ascribing to the collaboration between water-shielding EDL and stable SEI. Furthermore, in situ EIS after each Zn plating/stripping cycle was also explored (Supplementary Fig. 35). The impedance of the cell in 1 M $Zn(OTf)_2$ electrolyte fluctuates greatly during the Zn platting/stripping cycling process, which is attributable to the generation of Zn dendrites, "dead Zn" and the passivation of by-products, seriously hindering the stability and reversibility of the zinc anode[54]. Unlike that, the impedance of the cell using the electrolyte with 1 *wt*% PS tends to stabilize after experiencing small changes, ensuring steady Zn^{2+} transport kinetics and significantly reversible Zn plating/stripping process. In addition, the local pH variation near the Zn electrode would be attenuated in the electrolyte with 1 *wt*% PS during the deposition process, which further proves the suppressed HER on the Zn anode (Fig. 3l).

Structure characterization and formation mechanism of stable SEI

In-depth understanding of SEI chemistry and the correlation between EDL and SEI were explored using X-ray photoelectron spectroscopy (XPS), time-of-flight secondary ion mass spectrometry (TOF-SIMS), and high-resolution transmission electron microscopy (HRTEM). The XPS spectra indicate that SEI contains the C, F, S, and O elements. In the C 1*s* region (Fig. 4a), organic components (CF_3, C–O) with minor inorganic CO_3^{2-} species were also observed on the SEI surface. The small amount of inorganic CO_3^{2-} species might form from either of incomplete reduction of Zn^{2+}-anion and the dissolved CO_2 in electrolytes, which participates in the generation of $ZnCO_3$[55]. The CF_3 species originates from either of the incomplete reduction products of OTf^- anion or trace $Zn(OTf)_2$ residue on Zn surface[56], along with the feature in the F 1*s* region (Fig. 4b). Therefore, the topmost surface is mainly composed of organic components. Reduction of the OTf^- anion is confirmed by a peak at 684.6 eV assigned to ZnF_2, along with sulfites (169.1 eV), ZnS (162.4 eV) observed in the S 2*p* spectra (Fig. 4c), and SO_3^{2-}/CO_3^{2-} (532.1 eV) and ZnO (530.8 eV) detected in the O 1*s* region (Fig. 4d). Moreover, the element distribution across the SEI further confirms that the complex SEI consist of an organic-rich top layer and inorganic $ZnCO_3$-ZnO-ZnF_2-ZnS-rich inner layer (Supplementary Fig. 36), which will enhance Zn anode reversibility and regulate the uniform Zn deposition. The anion-derived and inorganic-rich SEI layer was also investigated by ToF-SIMS (Fig. 4e, f and Supplementary Fig. 37). According to the depth analysis curves, the contents of ZnF_2, ZnS, and $ZnCO_3$ on the Zn anode cycled in the electrolyte with 1 *wt*% PS are significantly higher than those in 1 M $Zn(OTf)_2$. Correspondingly, the 3D tomography of F^-, S^-, and CO_3^- ion fragments mainly distributes at the inner layer, suggesting a gradient of inorganic-rich SEI formed. The HRTEM image highlight the organic-inorganic hybrid compositions, where amorphous organic component as well as the lattice fringes of 0.29, 0.28, 0.27, and 0.26 nm can assign to ZnS (101), ZnO (100), $ZnCO_3$ (104) and ZnF_2 (101), respectively (Fig. 4g). The structure model and possible formation mechanism of SEI are built (Supplementary Fig. 38). When a complete SEI layer is formed, solvated Zn^{2+} diffuses from the electrolyte to the SEI surface and undergoes desolvation during plating. Subsequently, it penetrates into the SEI layer and finally reaches the Zn anode to complete the deposition reaction. The formation of a dense and stable organic-inorganic hybrid SEI may guide the preferential orientation of Zn deposition and suppress the detrimental reactions.

The energy levels of the highest occupied molecular orbital (HOMO) and the lowest unoccupied molecular orbital (LUMO) of PS and H_2O were examined to in-depth understand the Zn/electrolyte interface chemistry (Fig. 4h). Particularly, PS possesses a higher energy level of HOMO (−7.180 eV) than H_2O (−8.414 eV), suggesting that PS is easier to lose electrons and promote the electrons transfer from PS to Zn[57]. Moreover, the lower LUMO energy levels of PS (0.310 eV) than

https://doi.org/10.1038/s41467-025-59830-y

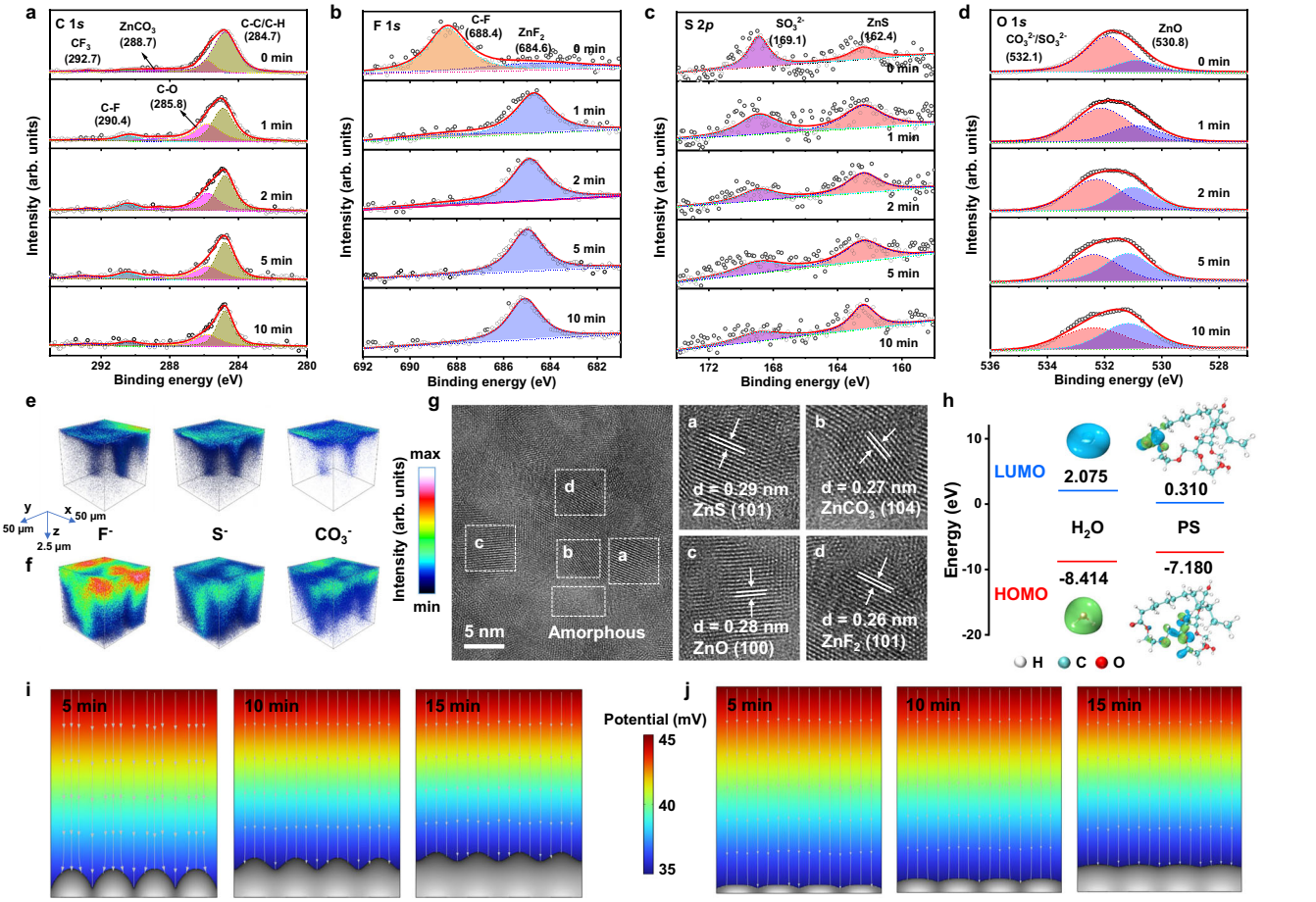

Fig. 4 | The structure characterization and formation mechanism of stable SEI. **a** C 1*s*, **b** F 1*s*, **c** S 2*p*, and **d** O 1*s* XPS spectra of the Zn anode after 50 cycles in electrolyte with 1 *wt*% PS. Spatial distribution of F^-, S^-, and CO_3^- on the Zn anode after 50 cycles in (**e**) 1 M $Zn(OTf)_2$ electrolyte and (**f**) electrolyte with 1 *wt*% PS detected by ToF-SIMS. **g** HRTEM images of the Zn anode after 50 plating/stripping cycles in electrolyte with 1 *wt*% PS. **h** LUMO, HOMO isosurfaces of H_2O and PS molecules. Simulated electric field distributions during the process of Zn deposition on the Zn electrode in (**i**) 1 M $Zn(OTf)_2$ and (**j**) electrolyte with 1 *wt*% PS.

H_2O (2.075 eV) suggest that PS tends to be preferentially reduced on the Zn anode. To deeply delve into the effect of PS addition on the dynamic electric field and surface morphology of the Zn anode during the plating/stripping processes, COMSOL Multiphysics simulations based on finite element modeling (FEM) were carried out in the scenario with or without PS additive. As the plating time increases from 5 to 15 min, the electric field is chaotic and enhanced intensity on the top of the crystal Zn seeds in 1 M $Zn(OTf)_2$ electrolyte, which results in the irregular Zn^{2+} bulges and random concentration (Fig. 4i). In sharp contrast, the introduction of PS gives rise to a homogeneous electric field, consequently inducing uniform Zn deposition over the deposition time (Fig. 4j). In the stripping process, the dendritic and irregular Zn stripping is observed in 1 M $Zn(OTf)_2$, while Zn anode surface in the electrolyte with 1 *wt*% PS shows ordered and planar stripping (Supplementary Fig. 39). These results illustrate that the PS adsorption layer can regulate the uniform distribution of electric field, avoid the tip effect and achieve ordered planar plating/stripping.

Long-term and highly utilized zinc metal anode

The Zn||Zn symmetric cells and Zn||Cu asymmetrical cells were assembled to evaluate the reversibility and cycling stability of the Zn anode in different electrolytes. As shown in Fig. 5a and Supplementary Fig. 40a, introducing 1 *wt*% PS additive delivers stable cycling stability and reversibility of Zn anodes. In addition, the Zn||Zn cell in the electrolyte with 1 *wt*% PS can perform a cycle lifespan of 8060 h (335 days) under 1 mA cm^{-2} and 1 mAh cm^{-2}, which is nearly 27 times that of 1 M $Zn(OTf)_2$ electrolyte (300 h). Even when cycled at high plating capacity of 5 and 10 mAh cm^{-2}, the high stability of 4554 and 1930 h, respectively. Moreover, the rate performance of the Zn||Zn cell shows a steadier voltage profile at various current densities in the electrolyte with 1 *wt*% PS (Fig. 5b, c). When the DOD_{Zn} increased to 68.3% under 40 mA cm^{-2} and 40 mAh cm^{-2}, the Zn anode in the electrolyte with 1 *wt*% PS achieved an extended cycle life of 450 h (Supplementary Fig. 40b). The Zn||Cu cell quickly fails with a sharp decline of Coulombic efficiency (CE) at high current density and high capacity (5 mA cm^{-2} and 5 mAh cm^{-2}) in the 1 M $Zn(OTf)_2$ electrolyte. In contrast, the Zn||Cu cell in the electrolyte with 1 *wt*% PS demonstrates a cycling stability over 600 cycles with a high average CE value of 99.3% (Fig. 5d). The corresponding capacity-voltage profiles with higher voltage polarization and steady voltage hysteresis also prove a reversible and stable Zn plating/stripping in the electrolyte with 1 *wt*% PS (Fig. 5e)[58]. In addition, the rate stability of the Zn||Cu cell under different current densities is also probed, where the cell in the electrolyte with 1 *wt*% PS has significantly improved the CE in the initial cycle and maintains high cycling stability from 0.5 to 10 mA cm^{-2} at 1 mAh cm^{-2} (Supplementary Fig. 41). The initial increase of CE should be attributed to the conditioning of the Cu foil surface and the formation of a stable SEI. Moreover, even if the zinc salt is changed from $Zn(OTf)_2$ to $ZnSO_4$, $Zn(TFSI)_2$, $ZnClO_4$, $ZnCl_2$, and $Zn(BF_4)_2$, the electrolytes incorporating PS molecules possess enhanced cycling stability and rate performance (Fig. 5f and Supplementary Figs. 42 and 43), indicating that PS as an additive is generally applicable to improve the reversibility and stability of zinc anode. The introduction of PS additive shows competitive electrochemical performance than most recent research (Fig. 5g, h and

https://doi.org/10.1038/s41467-025-59830-y

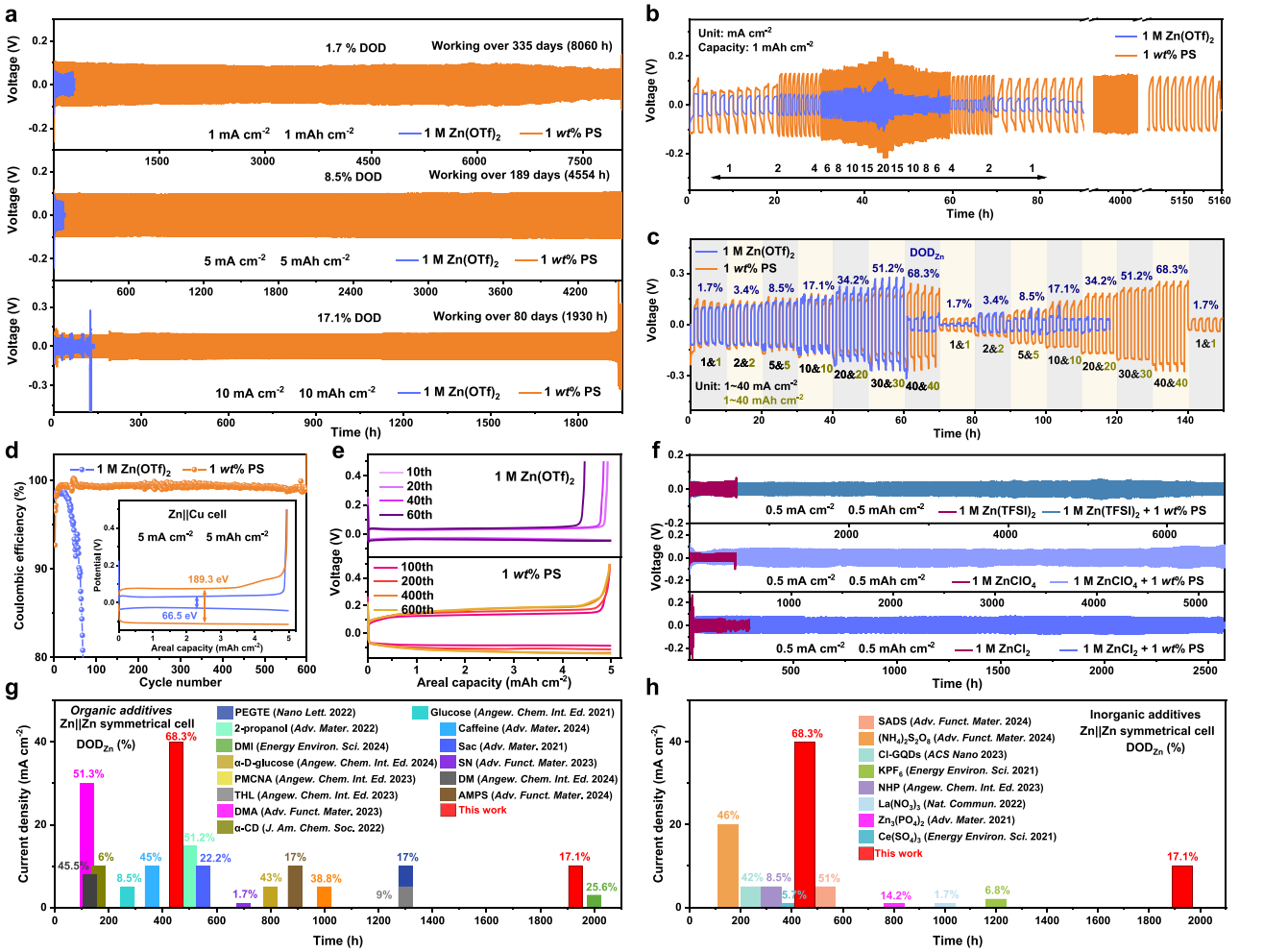

Fig. 5 | Long-term and highly utilized zinc metal anode. a The stripping/plating performance of Zn||Zn cells with 1 M $Zn(OTf)_2$ electrolyte and electrolyte with 1 *wt*% PS under various current densities and area capacities. **b**, **c** Rate performances of Zn||Zn cells during Zn stripping/plating with 1 M $Zn(OTf)_2$ electrolyte and electrolyte with 1 *wt*% PS. **d** CE measurements of asymmetric Zn||Cu cells with 1 M $Zn(OTf)_2$ electrolyte and electrolyte with 1 *wt*% PS at 5 mA cm^{-2} and 5 mAh cm^{-2}, and (**e**) corresponding voltage profiles at various cycles. **f** Galvanostatic cycling of Zn| |Zn cells in different electrolytes with PS additives at 0.5 mA cm^{-2} and 0.5 mAh cm^{-2}. **g**, **h** Comparison of cyclic reversibility in the recent reports, showing the current density, lifespan, and depth of discharge (DOD_{Zn}). The source of the literature data shown in these figures can be found in Supplementary Information, Tables 1 and 2.

Supplementary Tables 1–7). This performance demonstrates that the electrolyte with 1 *wt*% PS can effectively suppress side reactions and dendrites under high Zn utilization.

Assembly and performance study of full cells

To further evaluate the electrochemical performance and practicability of the PS additive, V_2O_5/rGO (Supplementary Fig. 44) and MnO_2 (Supplementary Fig. 45) were utilized as cathode materials to assemble Zn||V_2O_5/rGO and Zn||MnO_2 full cells, respectively. The galvanostatic charge discharge (GCD) curves (Supplementary Fig. 46) at different current densities show that Zn||V_2O_5/rGO full cell using the electrolyte with 1 *wt*% PS has higher reversible behavior and improved rate performance. At a low specific current of 0.2 A g^{-1}, the Zn||V_2O_5/rGO full cell with the electrolyte with 1 *wt*% PS exhibits a higher discharge capacity of 363.6 mAh g^{-1} compared to the capacity of 347.3 mAh g^{-1} in the 1 M $Zn(OTf)_2$ electrolyte (Fig. 6a). In particular, the cell with the electrolyte with 1 *wt*% PS delivers a fast capacitive-dominated charge storage mechanism and ascendant discharge capacity of 159.4 mAh g^{-1} at 10 A g^{-1} [59]. Moreover, the electrolyte with 1 *wt*% PS elegantly boosts the long-term durability and reversibility with an improved capacity retention of 81.1% after 3000 cycles at 5 Ag^{-1} (Fig. 6b). Overall, compared with the previously reported ZIBs, the Zn||V_2O_5/rGO full cell exhibited a large capacity and longer cyclic stability (Fig. 6c and Supplementary Table 8), owing to the PS-induced reversible plating/stripping electrochemistry. Additionally, the cycled Zn anode in 1 M $Zn(OTf)_2$ electrolyte is covered by cluttered dendrites and pulverization, while the Zn anode in the electrolyte with 1 *wt*% PS still maintains the initial morphology and ensures smooth transport of Zn^{2+} (Fig. 6d, e). Similarly, SEM images reveal that the cycled V_2O_5/rGO cathode in the electrolyte with 1 *wt*% PS maintains the initial morphology after 1000 cycles (Supplementary Fig. 47). However, obvious sheet-like by-products were generated in 1 M $Zn(OTf)_2$ electrolyte, which will impede ion transport, consume electrolyte, and reduce the reversibility of the battery. Moreover, the galvanostatic intermittent titration technique (GITT) further displays that the electrolyte with 1 *wt*% PS shows higher ion diffusion coefficients during the charge/discharge process (Fig. 6f and Supplementary Fig. 48), demonstrating the enhanced Zn^{2+} diffusion kinetics[60]. Notably, a significant improvement in self-discharge behavior was observed upon the introduction of PS. The full cell using the electrolyte with 1 *wt*% PS can still hold 95.5% of its original capacity, surpassing that using 1 M $Zn(OTf)_2$ electrolyte (79.6%) (Fig. 6g), which again indicates that the PS effectively suppresses side reactions and V-based oxide dissolution. More importantly, Zn||V_2O_5/rGO pouch cells are assembled to clarify

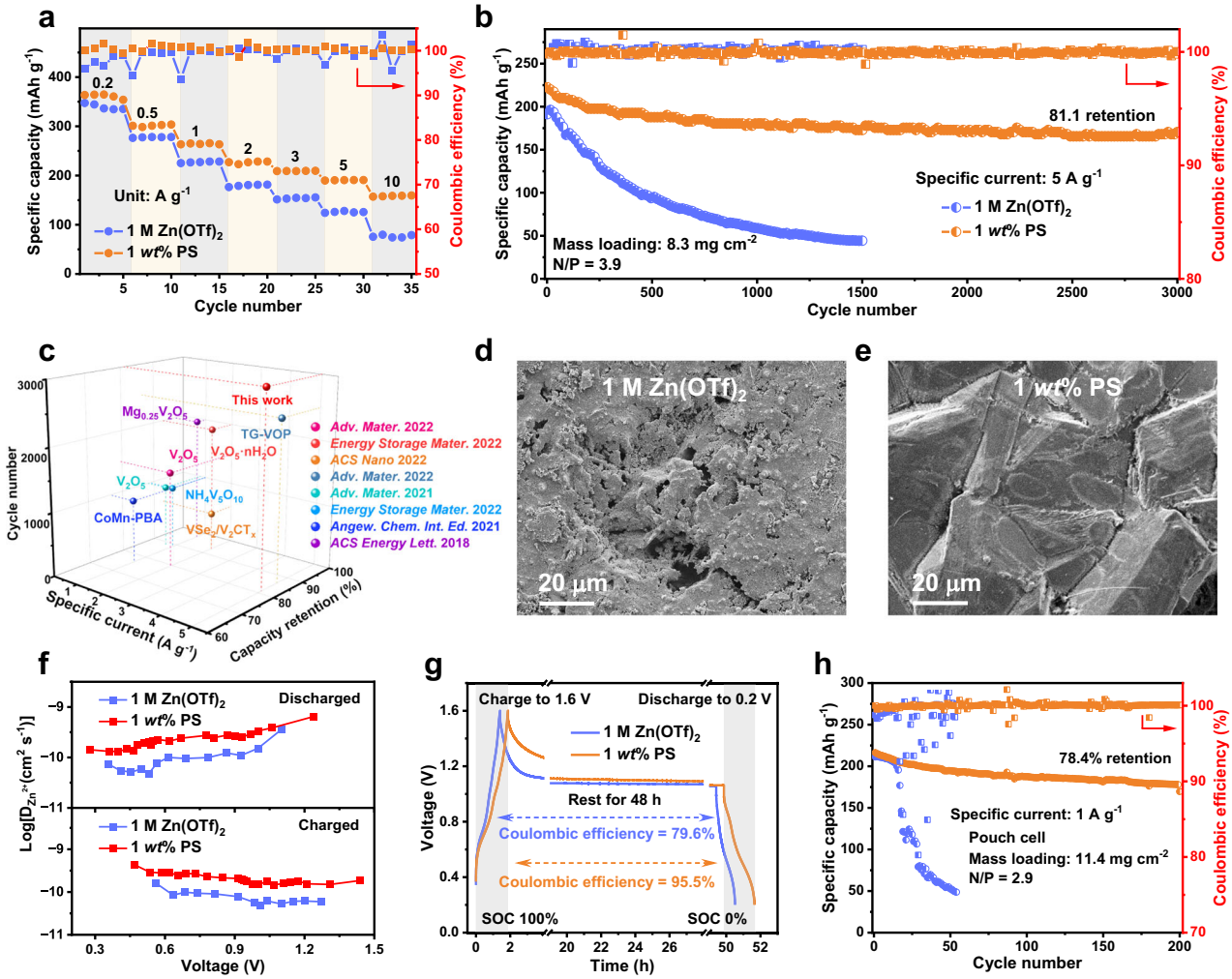

Fig. 6 | Electrochemical performance of full cell. a Rate performance of Zn||V_2O_5/rGO full cells using different electrolytes from 0.2 to 10 A g^{-1}, the mass loadings of V_2O_5/rGO are about 1.5 mg cm^{-2}. **b** Long-term cycling performance of Zn||V_2O_5/rGO full cells at 5 A g^{-1}. **c** Comparison of the cycling performance of the battery in this work with reported other ZIBs. The source of the literature data shown in this figure can be found in Supplementary Table 8. **d**, **e** SEM images of Zn anodes disassembled from Zn||V_2O_5/rGO full cells using different electrolytes after 1000 cycles at 5 A g^{-1}. **f** Zn^{2+} diffusion coefficients comparison in different electrolytes. **g** The self-discharge behavior of batteries with different electrolytes. **h** Cycling performance of Zn||V_2O_5/rGO pouch cells with different electrolytes.

the application prospect. The pouch cell with the electrolyte with 1 *wt*% PS delivers a high initial capacity of 216.3 mAh g^{-1} at 1 A g^{-1} and capacity retention of 78.4% after 200 cycles (Fig. 6h). Noteworthily, the pouch cell with 1 M $Zn(OTf)_2$ electrolyte shows significant swelling and gas evolution, while no signs of swelling were observed in the electrolyte with 1 *wt*% PS (Supplementary Fig. 49), confirming that PS significantly suppressed the side reactions. Furthermore, two serially connected pouch cells successfully drive a motor fan, providing tangible evidence of the great applicability potential of the designed ZIBs (Supplementary Fig. 50). Specifically, the electrolyte with 1 *wt*% PS manifests the positive influence of SEI. It exhibits improved temperature adaptability, and Zn plating/stripping behavior as well as long cycle stability are significantly improved at both −10 °C and 50 °C (Supplementary Figs. 51 and 52). Moreover, when replacing V_2O_5/rGO with MnO_2, another typically unstable cathode, the Zn||MnO_2 full cell in the electrolyte with 1 *wt*% PS also showed a higher reversible CE and enhanced cycling life of 81.9% capacity retention after 2000 cycles (Supplementary Fig. 53). The Ragone plots of Zn||V_2O_5/rGO and Zn||MnO_2 cells using the electrolyte with 1 *wt*% PS are shown in Supplementary Fig. 54 (based on the total mass of the cathode and anode), in which specific energy of 6.8 and 6.0 Wh kg^{-1} are obtained for Zn||V_2O_5/rGO and Zn||MnO_2 cells.

Discussion

In summary, a large-sized nonionic amphiphilic PS is proposed to construct water-shielding EDL and hybrid SEI for practical ZIBs. PS molecules do not participate in the Zn^{2+} solvation shell, but significantly homogenize the distribution of solvated Zn^{2+}. Simulation calculations and ex situ/in situ characterizations indicate that the PS molecules could produce preferential chemisorption and directional arrangement on the Zn anode, spontaneously forming water-shielding EDL and in situ constructing stable hybrid SEI. Tuned electrolyte increased anion decomposition on the anode, which further leads to an organic-rich top layer and an inorganic $ZnCO_3$-ZnO-ZnF_2-ZnS-rich inner layer. The synergistic effects between water-shielding EDL and hybrid SEI significantly suppress HER and chemical corrosion, as well as elegantly accelerate Zn^{2+} desolvation and guide dominant Zn (002) deposition to achieve ordered plating/stripping. As a result, the electrolyte with 1 *wt*% PS enables enhanced cycling life for 8060 h under 1 mA cm^{-2} and 1 mAh cm^{-2} (450 h at 40 mA cm^{-2}, 40 mAh cm^{-2}) in Zn||Zn cell, and highly reversible in Zn||Cu cell over 3900 cycles. More encouragingly, the full cells paired with V_2O_5/rGO and MnO_2 deliver the improved capacity and sustained stability. We anticipate that this work inspires a strategy for constructing stable interface chemistry to protect the metal anode, promoting practical applications of aqueous batteries.

Methods

Preparation of electrolytes and electrodes

The 1 M zinc trifluoromethanesulfonate ($Zn(OTf)_2$) aqueous electrolyte was prepared using $Zn(OTf)_2$ (98%, Sigma-Aldrich) and deionized water. Different amounts of polysorbate 20 (PS) (reagent grade, Aladdin Scientific Co., Ltd.) were added to 1 M $Zn(OTf)_2$ electrolyte, maintaining weight ratios of PS to H_2O at 0.25%, 0.5%, 1%, 2%, 5%, and 10% to prepare nonionic amphipathic polymer electrolytes and the corresponding electrolytes are denoted as 0.25 *wt*% PS, 0.5 *wt*% PS, 1 *wt*% PS, 2 *wt*% PS, 5 *wt*% PS, and 10 *wt*% PS, respectively. The electrolytes using zinc sulfate ($ZnSO_4$) (99%, Sigma-Aldrich), zinc bis(trifluoromethanesulfonyl)imide ($Zn(TFSI)_2$) (98%, Sigma-Aldrich), zinc perchlorate hexahydrate ($ZnClO_4$) (99.9%, Sigma-Aldrich), and zinc chloride ($ZnCl_2$) (98%, Sigma-Aldrich), zinc ditetrafluoroborate hydrate ($Zn(BF_4)_2$) (chemical pure, Sigma-Aldrich) salts as based salts were prepared with a similar method.

To prepare the V_2O_5/rGO cathode, 1.09 g V_2O_5 powder (99%, Sigma-Aldrich) and 2.27 g $C_2H_2O_4{\cdot}2H_2O$ powder (99%, Sigma-Aldrich) were added into 36 mL deionized water at 75 °C for 2 h to prepare the VOC_2O_4 solution. Then, the as-prepared VOC_2O_4 solution was dropped into 300 mL (1 mg mL^{-1}) graphene oxide dispersion (GO, Hangzhou Gaoxi Technology Co. Ltd.) and stirred for 2 h. Subsequently, the collected sample was freeze-dried and then annealed at 300 °C in flowing argon for 2 h to synthesize V_2O_5/rGO. To prepare the MnO_2 cathode, a precursor solution was prepared by combining 0.9 g of $KMnO_4$ (99%, Sigma-Aldrich) with 2 mL of concentrated HCl (37%, Sigma-Aldrich) in 80 mL deionized water. The mixture was continuously stirred magnetically for 30 min before undergoing hydrothermal reaction in a 100 mL Teflon-lined stainless-steel autoclave at 160 °C for 12 h. The resulting precipitate was washed and dried to obtain the final product. The cathode slurry was prepared via active materials, conductive carbon (Super P, Canrd Technology Co. Ltd.) and polyvinylidene fluoride (PVDF, Canrd Technology Co. Ltd.) in 7: 2: 1 mass ratio in N-methyl-2-pyrrolidone (NMP, 99.5%, Sigma-Aldrich) solution, then cast on a Ti foil (20 μm, Canrd Technology Co. Ltd.). The electrodes were punched into 10 mm disks after being dried at 60 °C overnight.

Assembly of cells

Electrolyte solutions were prepared a day before the cell assembly and stored in the dry cabinet (25 °C). For symmetric and asymmetric cell configurations (2032-type coin cells), which inherently include a stainless steel spacer (1.0 mm thickness), a spring-loaded plunger (stainless steel, 1.5 kN constant force), the working electrodes, and a glass fiber filter (Whatman GF/D) separator. For Zn||Zn symmetric cell, two pieces of Zn foils (99.9%, Canrd Technology Co. Ltd.) with a thickness of 100 μm were used as two electrodes. For Zn||Cu or Zn||Ti asymmetric cell, a Cu foil (20 μm thickness, Canrd Technology Co. Ltd.) or Ti foil (20 μm thickness, Canrd Technology Co. Ltd.) was used to replace one side of the Zn foil. The volume of the electrolyte was fixed to 80 μL. Zn||V_2O_5/rGO and Zn||MnO_2 full batteries were assembled by using V_2O_5/rGO, MnO_2 as cathodes, zinc foil as anode, and a glass fiber filter (Whatman GF/D) as the separator. The mass loadings of MnO_2 are about 1.5 mg cm^{-2} and 9.6 mg cm^{-2}. The mass loadings of V_2O_5@rGO in coin cells are about 1.5 mg cm^{-2} and 8.3 mg cm^{-2}. For the Zn||V_2O_5/rGO pouch cells (6 cm × 6 cm), the Zn foil thickness is 20 μm, and the mass loading of the cathode is 11.4 mg cm^{-2}. Two electrode layers were sandwiched, and the battery was then assembled by thermal sealing. The obtained pouch cell was rested for six hours before the electrochemical test.

Materials characterization

The morphology and structure features of the samples were investigated by a scanning electron microscope (JSM-6700F, JEOL), a 3D laser confocal scanning microscope (Leica TCS SP), and a field emission scanning electron microscope (JEOL JSM-7500F). Raman spectra were recorded via a high-resolution Raman spectrometer (XploRA PLUS, HORIBA Jobin Yvon SAS). Fourier transform infrared (FTIR) spectra were recorded on a Nicolet Nexus 670. The Nuclear Magnetic Resonance (NMR) experiments were performed by a 600 MHz Bruker Avance III spectrometer with a 5 mm probe. Two-dimensional synchrotron X-ray diffraction (2DGIXRD) and X-ray diffraction (XRD) patterns were conducted by the Bruker diffractometer (Bruker D8). Pole image data was sourced from a Rigaku Smartlab 3 kW, and the rotation axis was measured from 0 to 360°, and the tilt axis was measured from 0 to 75°. The contact angles of different electrolytes on the Zn electrode were measured by an optical contact angle system (DSA100, KRUSS). The in situ optical images were obtained on a polarizing microscope (BA300Pol-Motic). The Zeta potentials were collected using Zetasizer NANOZS90. Atomic force microscopy (AFM) and Kelvin probe force microscope (KPFM) experiments were carried out using Bruker multimode 8. The elemental composition of the samples was investigated by X-ray photoelectron spectroscopy (ESCALAB 250) and Time-of-Flight secondary ion mass spectrometry (PHI NanoTOFII). The X-ray absorption spectra (XAS) of the samples, encompassing both the X-ray absorption near-edge structure (XANES) and extended X-ray absorption fine structure (EXAFS), were measured at the Singapore Synchrotron Light Source (SSLS) center. A monochromator equipped with a pair of channel-cut Si (111) crystals was utilized for this purpose. The storage ring of the synchrotron operated at an energy of 2.5 GeV, with an average electron current maintained below 200 mA. Specifically, the authors would like to thank Shiyanjia Lab (www.shiyanjia.com) for the XAS analysis.

Electrochemical measurements

The linear sweep voltammetry (LSV), chronoamperometry (CA), electrochemical impedance spectroscopy (EIS), and cyclic voltammetry (CV) were tested using an electrochemical workstation (CHI760E, Shanghai, China). The LSV measurement was carried out at a scan rate of 1 mV s^{-1} in a two-electrode system where Ti foil was the working electrode, Zn foil was the reference electrode, and the counter electrode. Linear polarization measurements were carried out using a three-electrode system with Zn foil as the working electrode, Pt wire as the counter electrode, and Ag/AgCl as the reference electrode, respectively. CA plots were measured in Zn||Zn symmetric cells at an overpotential of −150 mV. The EIS was measured for Zn||Zn symmetric cells with different cycles under the frequency ranging from 0.1 to ~100 kHz on AutoLab PGSTAT302N until reaching a total of 61 data points. The EIS was measured for Zn||Zn symmetric cells with different temperatures under the frequency ranging from 0.1 to ~100 kHz on CHI760E until reaching a total of 73 data points. Zn foils with an area of 1 cm^2 are used in both Zn||Zn cells and Zn||Cu cells. The performances of Zn||Zn symmetric batteries and Zn||Cu asymmetric batteries, and full batteries were collected by NEWARE battery test system (CT-4008 T-5V50mA-164, Shenzhen, China) at 25 °C. The voltage window for Zn||V_2O_5/rGO and Zn||MnO_2 batteries is 0.2–1.6 V and 0.8–1.8 V, respectively. The GITT was implemented to investigate electrochemical reaction kinetics and zinc-ion diffusion behavior at a specific current of 50 mA g^{-1} and a charge/discharge time and interval of 30 min for each step. The procedure was continued until the discharge voltage reached 0.2 V. The procedure was repeatedly executed through consecutive charge/discharge cycles. Data points are acquired at 4-s intervals throughout the measurement period for diffusion coefficient calculation using the equation:

$$D_{Zn} = \frac{4}{\pi\tau}\left(\frac{m_B V_M}{M_B A}\right)^2\left(\frac{\Delta E_s}{\Delta E_\tau}\right)^2 \quad (1)$$

where τ represents the duration of current pulses applied during titration, m_B denotes active material mass (g), M_B is the molecular weight (g mol^{-1}) and V_M is the molar volume (cm^3 mol^{-1}), A is the

effective electrode/electrolyte interfacial area (cm^{-2}), ΔE_s is open-circuit potential variations between successive relaxation phases, ΔE_τ is the potential variations between galvanostatic charge/discharge.

For in situ mass variation monitoring, a quartz crystal microbalance (EQCM 10 M, Gamry) system combined with an electrochemical workstation (Interface 1010, Gamry) was configured in two-electrode mode. The working electrode comprised a gold-coated quartz resonator pre-deposited with zinc, while zinc foil served dual functions as both counter and reference electrodes. Tests were performed at a scan rate of 10 mV s^{-1}. The mass change at the EQCM electrode surface was calculated based on the Sauerbrey equation:

$$\Delta f = -C_f \times \Delta m \tag{2}$$

Where Δf is the observed frequency change in Hz, Δm is the change in mass per unit area, C_f is the sensitivity factor (56.6 ng·cm^{-2}·Hz^{-1} at 20 °C).

Molecular dynamics simulations

Molecular dynamics simulations were executed on the GROMACS software package[61] with the electrolyte system comprising 130 $Zn(OTF)_2$, 3 PS, and 5717 H_2O molecules. The molecules were inserted in a $6.4 \times 6.4 \times 6.4$ nm^3 simulation box randomly to build the initial configuration. The electrostatic interactions were evaluated via PME methods. During the simulation process, the steepest descent method was employed to minimize the energies of the initial configurations, thereby initializing each system. After this energy minimization step, a 200 picosecond (ps) MD simulation was performed within the NPT ensemble to pre-equilibrate the system. The simulation utilized a time step of 2 femtoseconds (fs). The temperature was incrementally increased in a linear fashion from 0 to 298 Kelvin (K) over the course of 200 ps and subsequently maintained at 298 K until the conclusion of this pre-equilibration phase. Subsequently, a production simulation lasting 50 nanoseconds (ns) was executed. Throughout all simulations, the v-rescale thermostat algorithm was used to maintain a constant temperature of 298 K. Meanwhile, the Parrinello–Rahman algorithm was applied to ensure that the pressure remained stable at 1 atmosphere (atm).

Density functional theory calculations

All DFT calculations were carried out using the Vienna Ab Initio Package (VASP). These calculations were based on the generalized gradient approximation (GGA), specifically adopting the Perdew-Burke-Ernzerhof (PBE) functional[62,63]. The projected augmented wave (PAW) method was selected to model the ionic cores and incorporate valence electrons. The calculations utilized a plane-wave basis set with a kinetic energy cutoff set at 450 electron volts (eV). To handle the partial occupancies of the Kohn–Sham orbitals, the Gaussian smearing technique was applied, with a smearing width of 0.05 eV. The geometry optimization conversions with forces on atoms and energy differences were smaller than 0.02 eV $Å^{-1}$ and 10^{-5} eV, respectively. A vacuum spacing of 18 Å was established in the direction perpendicular to the plane of the structure. All structural calculations were carried out using a gamma-centered k-point grid of $1 \times 1 \times 1$. The weak interaction was described by the DFT + D3 method using the empirical correction in Grimme's scheme. The electrostatic potential (ESP) was analyzed by the Multiwfn package and the VMD package. The adsorption energy (E_{ads}) was calculated using the following formula:

$$E_{ads} = E_{total} - E_{substrate} - E_{adsorbate} \tag{3}$$

The E_{total}, $E_{substrate}$, and $E_{adsorbate}$ represent the energy of adsorption structure, substrate, and adsorbate (PS/H_2O molecule), respectively.

The Gaussian 16, C01 software package was employed to perform the desolvation energy calculations. The hybrid functional PBE0 functional was adopted for all calculations in combination with the D3 version of Grimme's dispersion with Becke–Johnson damping (DFT-D3BJ)[64,65]. For geometry optimization and frequency calculations, the def2-SVP basis set was used with the integral-equation-formalism polarizable continuum model (IEF-PCM) solvation model for water[66]. The singlet point energy calculations were performed with the def2-TZVP basis set, and the solvation model density implicit solvation model, was used to account for the water solvation effect.

COMSOL simulations

Finite Element Analysis (FEA) model was performed using COMSOL Multiphysics with the "Tertiary Current Distribution" and "Phase Field" modules to simulate the dynamic Zn deposition on electrodes in different electrolytes[67]. The size of the entire two-dimensional model was set to 2.0×1.5 μm. A transient simulation of the deposition process was conducted in a region filled with the electrolyte. The current density was specified at 1 mA cm^{-2}, and the plating/stripping process was modeled through the application of the phase field method. The diffusion of ion concentrations follows Fick's first law, and the reaction at the electrode surface follows the Butler–Volmer equation. The Zn^{2+} transfers by the concentration diffusion in the model follow Fick's law as shown in equations:

$$N_i = J_i = -D_i \nabla C_i \tag{4}$$

$$\frac{\partial_{C_i}}{\partial_t} + \nabla J_i = R_{i,tot} \tag{5}$$

Where J_i is the ion flux, D_i is the diffusion coefficient of electrolytes, c_i is the ion concentration of electrolytes, ∇c_i is the concentration gradient.

The relation between the diffusion coefficient and electric mobility follows the Nernst–Einstein relation as shown in the equation:

$$N_i = -D_i \nabla c_i - z_i \mu_{m,i} F c_i \nabla \phi_l + \mu c_i = J_i + \mu C_i \tag{6}$$

Where z_i is the transfer number, $u_{m,i}$ is the electric mobility coefficient, F is the Faraday constant (96485 C mol^{-1}), ϕ is the electrolyte potential.

The reaction at the electrode surface follows the Butler-Volmer equation:

$$i_{loc} = i_0 \left(\exp\left(\frac{\alpha_a F_\eta}{RT}\right) - \exp\left(\frac{-\alpha_a F_\eta}{RT}\right) \right) \tag{7}$$

Where i_{loc} is the local current density at the electrode/electrolyte interface, i_O is the exchange current density, α is the charge transfer coefficient, and η is the activation overpotential.

Data availability

The data that support the findings of this study are available from the corresponding author upon request. Source data are provided with this paper.

References

1. Wang, Y. et al. Manipulating electric double layer adsorption for stable solid-electrolyte interphase in 2.3 Ah Zn-pouch. *Cells Angew. Chem. Int. Ed.* **62**, e202302583 (2023).
2. Hao, J. et al. Advanced cathodes for aqueous Zn batteries beyond Zn^{2+} intercalation. *Chem. Soc. Rev.* **53**, 4312–4332 (2024).
3. Wang, F. et al. Production of gas-releasing electrolyte-replenishing Ah-scale zinc metal pouch cells with aqueous gel electrolyte. *Nat. Commun.* **14**, 4211 (2023).

4. Peng, Z. et al. Coupling uniform pore size and multi-chemisorption sites: hierarchically ordered porous carbon for ultra-fast and large zinc ion storage. *Adv. Funct. Mater.* **33**, 2303205 (2023).
5. Deng, Q. et al. Polymer molecules adsorption-induced zincophilic-hydrophobic protective layer enables highly stable Zn metal anodes. *Adv. Mater.* **36**, 2312924 (2024).
6. Zhang, Q. et al. Halogenated Zn^{2+} solvation structure for reversible Zn metal batteries. *J. Am. Chem. Soc.* **144**, 18435–18443 (2022).
7. Niu, B. et al. Nano-scaled hydrophobic confinement of aqueous electrolyte by a nonionic amphiphilic polymer for long-lasting and wide-temperature Zn-based energy storage. *Energy Environ. Sci.* **16**, 1662–1675 (2023).
8. Parker, J. et al. Rechargeable nickel-3D zinc batteries: an energy-dense, safer alternative to lithium-ion. *Science* **356**, 415–418 (2017).
9. Yang, Z. et al. A semi-solid zinc powder-based slurry anode for advanced aqueous zinc-ion batteries. *Angew. Chem. Int. Ed.* **62**, e202215306 (2023).
10. Zhang, M. et al. Construction of mixed ionic-electronic conducting scaffolds in Zn powder: a scalable route to dendrite-free and flexible Zn anodes. *Adv. Mater.* **34**, 2200860 (2022).
11. Meng, H. et al. Lamellar nanoporous metal/intermetallic compound heterostructure regulating dendrite-free zinc electrodeposition for wide-temperature aqueous zinc-ion battery. *Adv. Mater.* **36**, 2403803 (2024).
12. Zhang, X. et al. Single [0001]-oriented zinc metal anode enables sustainable zinc batteries. *Nat. Commun.* **15**, 2735 (2024).
13. Ren, L. et al. Suppressing metal corrosion through identification of optimal crystallographic plane for Zn batteries. *Proc. Natl. Acad. Sci. USA* **12**, e2309981121 (2024).
14. Mu, Y. et al. 3D hierarchical graphene matrices enable stable Zn anodes for aqueous Zn batteries. *Nat. Commun.* **14**, 4205 (2023).
15. Zheng, Z. et al. A functional Janus Ag nanowires/bacterial cellulose separator for high-performance dendrite-free zinc anode under harsh conditions. *Adv. Mater.* **35**, 2304667 (2023).
16. Li, Y. et al. Functional ultrathin separators proactively stabilizing zinc anodes for zinc-based energy storage. *Adv. Mater.* **35**, 2300019 (2023).
17. Zhang, X. et al. An ion-sieving Janus separator toward planar electrodeposition for deeply rechargeable Zn-metal anodes. *Adv. Mater.* **34**, 2205175 (2022).
18. Wu, G. et al. Extension of aqueous zinc battery life using a robust and hydrophilic polymer separator. *Adv. Funct. Mater.* **34**, 2316619 (2024).
19. Xue, R. et al. Multiscale interfacial regulation of Zn-V_2O_5 pouch cell via ultrathin molecular-engineered separator. *Adv. Funct. Mater.* **34**, 2400959 (2024).
20. Ai, Y. et al. Biomimetic superstructured interphase for aqueous zinc-ion batteries. *J. Am. Chem. Soc.* **146**, 15496–15505 (2024).
21. Cao, J. et al. In-situ ultrafast construction of zinc tungstate interface layer for highly reversible zinc anodes. *Angew. Chem. Int. Ed.* **63**, e202319661 (2024).
22. Chen, S. et al. Ordered planar plating/stripping enables deep cycling zinc metal batteries. *Sci. Adv.* **10**, eadn2265 (2024).
23. Wang, F. et al. Highly reversible zinc metal anode for aqueous batteries. *Nat. Mater.* **17**, 543–549 (2018).
24. Meng, C. et al. A eutectic electrolyte for an ultralong-lived Zn//V_2O_5 cell: anin situgenerated gradient solid-electrolyte interphase. *Energy Environ. Sci.* **16**, 3587–3599 (2023).
25. Chen, R. et al. Rational design of an in-situ polymer-inorganic hybrid solid electrolyte interphase for realising stable Zn metal anode under harsh conditions. *Angew. Chem. Int. Ed.* **136**, e20240198 (2024).
26. Xu, P. et al. In-situ solid electrolyte interface via dual reaction strategy for highly reversible zinc anode. *Angew. Chem. Int. Ed.* **63**, e202407909 (2024).
27. Liu, H. et al. Navigating fast and uniform zinc deposition via a versatile metal-organic complex interphase. *Energy Environ. Sci.* **15**, 1872–1881 (2022).
28. Qin, S. et al. Formulating self-repairing solid electrolyte interface via dynamic electric double layer for practical zinc ion batteries. *Angew. Chem. Int. Ed.* **63**, e202410422 (2024).
29. Wang, N. et al. Zincophobic electrolyte achieves highly reversible zinc-ion batteries. *Adv. Funct. Mater.* **33**, 2300795 (2023).
30. Cao, H. et al. Unraveling the solvation structure and electrolyte interface through carbonyl chemistry for durable and dendrite-free Zn anode. *Adv. Funct. Mater.* **33**, 2305683 (2023).
31. Weng, J. et al. Enhancing Zn-metal anode stability: key effects of electrolyte additives on ion-shield-like electrical double layer and stable solid electrolyte interphase. *Adv. Funct. Mater.* **34**, 2314347 (2024).
32. Dou, H. et al. Steric-hindrance effect tuned ion solvation enabling high performance aqueous zinc ion batteries. *Angew. Chem. Int. Ed.* **136**, e202401974 (2024).
33. Zhao, K. et al. Boosting the kinetics and stability of Zn anodes in aqueous electrolytes with supramolecular cyclodextrin additives. *J. Am. Chem. Soc.* **144**, 11129–11137 (2022).
34. Li, M. et al. Comprehensive H_2O molecules regulation via deep eutectic solvents for ultra-stable zinc metal anode. *Angew. Chem. Int. Ed.* **62**, e202215552 (2023).
35. Ren, H. et al. Molecular-crowding effect mimicking cold-resistant plants to stabilize the zinc anode with wider service temperature range. *Adv. Mater.* **35**, 2208237 (2023).
36. Li, G. et al. A biocompatible electrolyte enables highly reversible Zn anode for zinc ion battery. *Nat. Commun.* **14**, 6526 (2023).
37. Kim, M. et al. Surface overpotential as a key metric for the discharge-charge reversibility of aqueous zinc-ion batteries. *J. Am. Chem. Soc.* **145**, 15776–15787 (2023).
38. Li, B. et al. Multicomponent copper-zinc alloy layer enabling ultra-stable zinc metal anode of aqueous Zn-ion battery. *Angew. Chem. Int. Ed.* **134**, e202212587 (2022).
39. Kwon, M. et al. Stimulating Cu-Zn alloying for compact Zn metal growth towards high energy aqueous batteries and hybrid supercapacitors. *Energy Environ. Sci.* **15**, 2889–2899 (2022).
40. Bayaguud, A. et al. Cationic surfactant-type electrolyte additive enables three-dimensional dendrite-free zinc anode for stable zinc-ion batteries. *ACS Energy Lett.* **5**, 3012–3020 (2020).
41. Wei, T. et al. Building near-unity stacked (002) texture for high-stable zinc anode. *Adv. Funct. Mater.* **34**, 2312506 (2024).
42. Shen, Z. et al. Electrocrystallization regulation enabled stacked hexagonal platelet growth toward highly reversible zinc anodes. *Angew. Chem. Int. Ed.* **62**, e202218452 (2023).
43. Zhou, M. et al. Surface-preferred crystal plane for a stable and reversible zinc anode. *Adv. Mater.* **33**, 2100187 (2021).
44. Chang, C. et al. A robust gradient solid electrolyte interphase enables fast Zn dissolution and deposition dynamics. *Energy Environ. Sci.* **17**, 680–694 (2024).
45. Zhang, M. et al. Dynamically interfacial pH-buffering effect enabled by N-methylimidazole molecules as spontaneous proton pumps toward highly reversible zinc-metal anodes. *Adv. Mater.* **35**, 2208630 (2023).
46. Shi, M. et al. Molecule engineering of sugar derivatives as electrolyte additives for deep-reversible Zn metal anode. *Angew. Chem. Int. Ed.* **63**, e202407261 (2024).
47. Peng, H. et al. Dynamic Zn/electrolyte interphase and enhanced cation transfer of sol electrolyte for all-climate aqueous zinc metal batteries. *Angew. Chem. Int. Ed.* **62**, e202308068 (2023).
48. Peng, Z. et al. Hierarchically nitrogen-doped mesoporous carbon nanospheres with dual ion adsorption capability for superior rate and ultra-stable zinc ion hybrid supercapacitors. *Sci. China Mater.* **65**, 2401–2411 (2022).

49. Chu, Y. et al. In situ built interphase with high interface energy and fast kinetics for high performance Zn metal anodes. *Energy Environ. Sci.* **14**, 3609–3620 (2021).
50. Tang, D. et al. Switching hydrophobic interface with ionic valves for reversible zinc batteries. *Adv. Mater.* **36**, 2406071 (2024).
51. Zhou, J. et al. Diminishing interfacial turbulence by colloid-polymer electrolyte to stabilize zinc ion flux for deep-cycling Zn metal batteries. *Adv. Mater.* **34**, 2200131 (2022).
52. Wang, H. et al. Toward simultaneous dense zinc deposition and broken side-reaction loops in the Zn||V_2O_5 system. *Angew. Chem. Int. Ed.* **63**, e202318928 (2024).
53. Liu, S. et al. Monolithic phosphate interphase for highly reversible and stable Zn metal anode. *Angew. Chem. Int. Ed.* **62**, e202215600 (2023).
54. Cheng, Y. Manipulating Zn 002 deposition plane with zirconium ion crosslinked hydrogel electrolyte toward dendrite free Zn metal anodes. *Energy Environ. Sci.* **16**, 4561–4571 (2023).
55. Cao, L. et al. Fluorinated interphase enables reversible aqueous zinc battery chemistries. *Nat. Nanotechnol.* **16**, 902–910 (2021).
56. Li, C. et al. Enabling selective zinc-ion intercalation by a eutectic electrolyte for practical anodeless zinc batteries. *Nat. Commun.* **14**, 3067 (2023).
57. Yu, H. A functional organic zinc-chelate formation with nanoscaled granular structure enabling long-term and dendrite-free Zn anodes. *ACS Nano* **16**, 9736–9747 (2022).
58. Hao, J. et al. Boosting zinc electrode reversibility in aqueous electrolytes by using low-cost antisolvents. *Angew. Chem. Int. Ed.* **60**, 7366–7375 (2021).
59. Brezesinski, T. et al. Ordered mesoporous α-MoO_3 with iso-oriented nanocrystalline walls for thin-film pseudocapacitors. *Nat. Mater.* **9**, 146–151 (2010).
60. Zong, Q. et al. Dual effects of metal and organic ions co-intercalation boosting the kinetics and stability of hydrated vanadate cathodes for aqueous zinc-ion batteries. *Adv. Energy Mater.* **13**, 2301480 (2023).
61. Hes, B. et al. GROMACS 4: algorithms for highly efficient, load-balanced, and scalable molecular simulation. *J. Chem. Theory Comput.* **4**, 435–447 (2008).
62. Kresse, G. et al. Efficient iterative schemes for ab initio total-energy calculations using a plane-wave basis set. *Phys. Rev. B* **54**, 11169–11186 (1996).
63. Perdew, J. & Ernzerhof, M. Generalized gradient approximation made simple. *Phys. Rev. Lett.* **77**, 3865–3868 (1996).
64. Adamo, C. et al. Toward reliable density functional methods without adjustable parameters: the PBE0 model. *J. Chem. Phys.* **110**, 6158–6170 (1999).
65. Grimme, S. et al. Effect of the damping function in dispersion corrected density functional theory. *J. Comput. Chem.* **32**, 1456–1465 (2011).
66. Weigend, F. et al. Balanced basis sets of split valence, triple zeta valence and quadruple zeta valence quality for H to Rn: design and assessment of accuracy. *Phys. Chem. Chem. Phys.* **7**, 3297–3305 (2005).
67. Wang, D. et al. Solvation modulation enhances anion-derived solid electrolyte interphase for deep cycling of aqueous zinc metal batteries. *Angew. Chem. Int. Ed.* **62**, e202310290 (2023).

Acknowledgements

The authors would like to thank the support from the National Key R&D Program of China: Strategic International Innovation Cooperation (2024YFE0209400) received by Y.-W.C., the Postdoctoral Fellowship Program of CPSF (GZC20231027) and China Postdoctoral Science Foundation (2024M761262) received by Z.-Y.P., National Natural Science Foundation of China (52373186) and Key Project of Jiangxi Provincial Natural Science Foundation (20224ACB203007) received by L.-C.T.

Author contributions

Z.-Y.P. conceived the project, synthesized the materials, performed electrochemical testing, analyzed the data, and wrote the manuscript. S.-L.L., L.T., and J.-Y.Z. contributed to the structural characterizations and the data collection. Z.-Y.P., L.-C.T., and Y.-W.C. acquired funding. Z.-Y.P., L.-C.T., and Y.-W.C. contributed to the discussion of results and revised the manuscript. The manuscript was written through the contributions of all authors.

Competing interests

The authors declare no competing interests.

Additional information

Supplementary information The online version contains supplementary material available at https://doi.org/10.1038/s41467-025-59830-y.

Correspondence and requests for materials should be addressed to Licheng Tan or Yiwang Chen.

Peer review information *Nature Communications* thanks Jianchao Sun and the other anonymous reviewers for their contribution to the peer review of this work. A peer review file is available.